SCIENTIFIC REPORTS

OPEN

SUBJECT AREAS:
NANOSTRUCTURES
BIOINSPIRED MATERIALS

Received
1 October 2013

Accepted
2 December 2013

Published
18 December 2013

Correspondence and requests for materials should be addressed to F.Z. (zhang_fan@fudan.edu.cn) or D.Y.Z. (dyzhao@fudan.edu.cn)

Nd^{3+} Sensitized Up/Down Converting Dual-Mode Nanomaterials for Efficient *In-vitro* and *In-vivo* Bioimaging Excited at 800 nm

Xiaomin Li, Rui Wang, Fan Zhang, Lei Zhou, Dengke Shen, Chi Yao & Dongyuan Zhao

Department of Chemistry and Laboratory of Advanced Materials, Fudan University, Shanghai 200433, P.R. China.

Core/shell1/shell2/shell3 structured $NaGdF_4$:Nd/$NaYF_4$/$NaGdF_4$:Nd,Yb,Er/$NaYF_4$ nanocrystals were well designed and synthesized, each of the parts assume respective role and work together to achieve dual-mode upconverting (UC) and downconverting (DC) luminescence upon the low heat effect 800-nm excitation. Nd^{3+}, Yb^{3+}, Er^{3+} tri-doped $NaGdF_4$:Nd,Yb,Er UC layer [NIR (800 nm)-to-Visible (540 nm)] with a constitutional efficient 800 nm excitable property were achieved for the *in-vitro* bioimaging with low auto-fluorescence and photo-damage effects. Moreover, typical NIR (800 nm)-to-NIR (860–895 nm) DC luminescence of Nd^{3+} has also been realized with this designed nanostructure. Due to the low heat effect, high penetration depth of the excitation and the high efficiency of the DC luminescence, the *in-vivo* high contrast DC imaging of a whole body nude mouse was achieved. We believe that such dual-mode luminescence NCs will open the door to engineering the excitation and emission wavelengths of NCs and will provide a new tool for a wide variety of applications in the fields of bioanalysis and biomedical.

The development of nanoprobes for luminescence imaging is an area that is currently attracting considerable interests across a wide range of science, engineering, and biomedical disciplines[1,2]. Besides high quantum yield, good photostability, low toxicity, ideal luminescence probes for *in-vitro* and *in-vivo* bioimaging should also possess the appropriate spectral range for excitation/emission wavelengths. It has been demonstrated that "near-infrared (NIR) biological window" for both excitation and emission in the range of 650–900 nm not only can allow for low auto-fluorescence and reduced photo-damage effects but also offers deep light penetration and low light scattering[3–5]. Hence, for *in-vitro* imaging (such as cell labeling), the upconverting (UC) visible emission promoted by NIR excitation is always preferred (such as the UC green emission of $NaYF_4$:Yb,Er), because the NIR excitation could reduce the auto-fluorescence and photo-damage effects[6–8]. Most importantly, the visible emission is very convenient and visually intuitive for the observations with the naked eyes or widely equipped Si-CCD cameras of the microscope. For *in-vivo* imaging, it has been demonstrated that NIR-to-NIR downconverting (DC) emission is undisputed the best choice due to its high quantum yield compared to UC process, large penetration depth, high contrast and signal-to-noise ratio[9–11].

Owing to the unique luminescence properties, lanthanide ion-doped nanocrystals (NCs) have become a specific topic of interest in recent years. Compared with the conventional biological labels, such as organic dye markers and quantum dots, lanthanide ion-doped luminescent NCs have many advantages, including low photobleaching, narrow emission bands, long luminescent lifetimes and low long-term cytotoxicity[12–22]. Up to now, numerous lanthanide-doped nanomaterials have been developed, which can emit strong UC or DC luminescence by tuning different lanthanide dopants[23–26]. However, up to now it's still difficult to realize efficient nanoprobes with combined UC and DC dual-mode functions under the single NIR excitation and fulfill the excitation/emission wavelength requirements of the *in-vitro* and *in-vivo* applications mentioned above at the same time. Furthermore, for the UC process, because of well-established efficient UC luminescence, considerable efforts have been devoted to the synthesis of lanthanide-doped $NaYF_4$ ($NaGdF_4$) NCs, where Yb^{3+} acting as the sensitizer with a large absorption cross-section around 980 nm is usually co-doped along with the most common UC activator ions (Er^{3+}, Tm^{3+}, Ho^{3+}, Pr^{3+} and Tb^{3+}) to produce strong visible and violet emissions. However, it is worth pointing out that excitation light around 980 nm suffers from an intrinsic disadvantage: water, as the most significant component of the cell, animal and human body, has a huge absorption peak around 980 nm

(Figure S1), which would be overwhelmingly attenuated while diffusing in the biological samples. Moreover, almost all the 980-nm excitation energy absorbed by biological samples would be transformed into local heating energy, which could probably induce heat damages for the cells and tissues[3–5,27]. The heat effect and limited penetration depth will seriously affect the *in-vitro* and *in-vivo* bioimaging efficiency and application extension. Therefore, further optimization in the excitation mode is really desired for the bioapplications of UC nanomaterials. As can be noticed in reported "NIR biological window", the local minimum of water absorption is at around 800 nm (Figure S1), which has been considered to be the ideal excitation wavelength with the least impact on biological tissues[3–5].

Recently, the Nd^{3+} ion is considered as a good candidate for improving the pumping efficiency of 800-nm laser diode, due to its intense absorption cross-section around 800 nm[28,29]. Interestingly, Yb^{3+} ions can play a role of an energy-transfer bridging ions between an energy donor (Nd^{3+}) ion and energy acceptor RE^{3+} ions (Er^{3+}, Tm^{3+}, Ho^{3+}, Pr^{3+} and Tb^{3+}) under excitation at 800 nm[30–32]. Up to now, the Nd^{3+}-Yb^{3+}-RE^{3+} system has been explored in glass hosts under 800-nm excitation. If this Nd^{3+} ion sensitized UC system can be realized in the nanomaterials, it could further push forward the bioapplications of UC system with less heat effect and better tissue penetration properties[39–41]. Furthermore, the DC luminescence of Nd^{3+} doped bulk materials has also been extensively investigated such as the excellent laser medium due to the large absorption cross section and high optical conversion efficiency (~53%)[32–34]. Therefore, if we can engineer the nanostructure of the nanomaterials with both above mentioned Yb^{3+}-Nd^{3+}-RE^{3+} UC system and Nd^{3+} doped DC system at the same time, we could realize the Nd^{3+} sensitized UC/DC dual-mode nanoprobe under the single excitation around 800 nm with the low heat effect and highly efficient bioimaging function. In this paper, we demonstrate a strategy to fabricate uniform multi-layer core/shell1/shell2/shell3 (C/S1/S2/S3) β-$NGdF_4$:Nd/$NaYF_4$/$NaGdF_4$:Nd,Yb,Er/$NaYF_4$ NCs that are composed of the $NaGdF_4$:Nd core (DC) and the $NaGdF_4$:Nd,Yb,Er shell (S2) (UC) in order to achieve dual-mode luminescence under the single excitation around 800 nm (Figure 1). This kind of NCs could serve as multiplexed luminescent biolabel for both *in-vitro* and *in-vivo* bioimaging applications.

Results

As shown in Figure 1, the single nanoparticle is consisted of four parts, each of the parts assume respective role and work together to fulfill the dual-mode luminescence. It has been demonstrated that Nd^{3+} possesses intense absorption cross-section at around 800 nm (Figure S2) and highly efficient NIR-to-NIR DC luminescence (quantum yield ~ 40%) could be obtained when the Nd^{3+} activator was used in the nanomaterials[35]. Therefore, in the present designed nanostructure the $NaGdF_4$:Nd was constructed as a core for emitting the NIR DC luminescence under 800-nm excitation. This NIR-to-NIR DC luminescence is ideal for *in-vivo* applications with deep light penetration, low light scattering and heat effect because both the exciting and emission wavelength were located in the "NIR biological window". For the UC luminescence, unlike the typically used single sensitizer (Yb^{3+}) upconversion system, efficient 800-nm excited NIR-to-Visible UC emission of Er^{3+} is realized (shell 2) by taking advantage of Nd^{3+} and Yb^{3+} ions as double sensitizers, which can be used for the efficient *in-vitro* bioimaging with a low auto-fluorescence and reduced photo-damage effects. Furthermore, we also found that there is competitive relationship between the DC and UC due to the energy transfer, which are governed by the law of conservation of energy. Hence, in order to avoid the energy transfer between the DC core and UC shell2, a $NaYF_4$ host layer (shell1) was inserted. Moreover, as we all know, a major deleterious factor in regard to luminescence of colloidal NCs is the energy traps on their

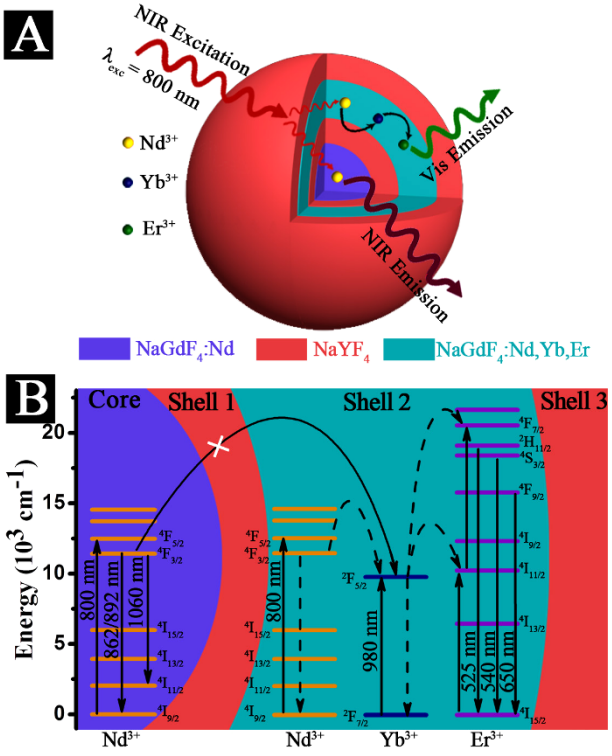

Figure 1 | (A) General strategy to achieve the UC and DC dual-mode luminescence with multi-layer C/S1/S2/S3 β-$NGdF_4$:Nd/$NaYF_4$/$NaGdF_4$:Nd,Yb,Er/$NaYF_4$ NCs. (B) Proposed energy transfer mechanisms in the multi-layer core/shell NCs.

surface, which includes sublattice defects and external deactivators. Therefore, to make sure the photostability of the UC (shell 2) a $NaYF_4$ host layer (shell 3) was also designed fabricated on the outmost of the particle to minimize the defects and external deactivators.

The successive layer-by-layer (SLBL) strategy reported previously by our group was introduced for the syntheses of the C/S1/S2/S3 β-$NaGdF_4$:Nd/$NaYF_4$/$NaGdF_4$:Nd,Yb,Er/$NaYF_4$ NCs[36]. Transmission electron microscopy (TEM) images of the resultant NCs before and after the shell1, shell2, shell3 growth show that the nearly monodispersed and uniform $NaGdF_4$:Nd cores with an average diameter of 10 ± 1 nm are gradually grown into 14 ± 0.8, 17 ± 1 and 20 ± 1.2 nm core/shell NCs after the successive growth of $NaYF_4$ insert layer, $NaGdF_4$:Nd,Yb,Er UC layer and $NaYF_4$ passivation layer, respectively. The high-resolution TEM (HRTEM) images along with the corresponding fast Fourier transform (FFT, Figure 2E–H) of the resultant NCs before and after shell1, shell2, shell3 successive coating show similar lattice fringes and FFT patterns. It indicates that all the obtained NCs are highly crystalline and maintain the same hexagonal crystal structure during the synthesis process, which also can be confirmed by the results of the X-ray diffraction results (XRD) (Figure S3). The increase of the particle size along with maintained uniform morphology primarily suggests the success growth of the premeditated shells. Considering the difference in atomic weight between Y and Gd in the obtained NCs, high-angle annular dark-field scanning transmission electron microscopy (HAADF-STEM) was employed to identify the formation of the core/shell structure by image contrast. All the HAADF-STEM images of $NaGdF_4$:Nd/$NaYF_4$ (C/S1) (Figure 2I), $NaGdF_4$:Nd/$NaYF_4$/$NaGdF_4$:Nd,Yb,Er (C/S1/S2) (Figure 2J) and $NaGdF_4$:Nd/$NaYF_4$/$NaGdF_4$:Nd,Yb,Er/$NaYF_4$ (C/S1/S2/S3) (Figure 2K) NCs show a discernible contrast, in which the brighter parts correspond to the heavier Gd elements and the darker parts correspond to the lighter Y elements. Taking the C/S1/S2/S3 NCs as an example (Figure 2L), clearly multi-layer

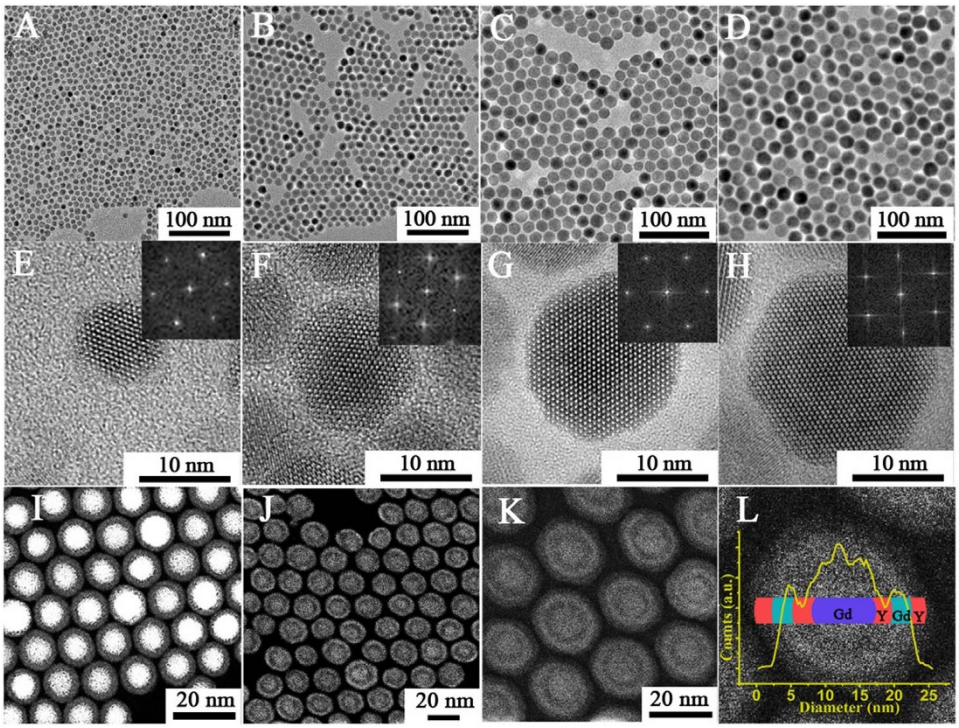

Figure 2 | TEM (A–D) and HRTEM (E–H) images of $NaGdF_4$:Nd core (A), (E), $NaGdF_4$:Nd/$NaYF_4$ (B), (F), $NaGdF_4$:Nd/$NaYF_4$/$NaGdF_4$:Nd,Yb,Er (C), (G) and $NaGdF_4$:Nd/$NaYF_4$/$NaGdF_4$:Nd,Yb,Er/$NaYF_4$ (D, H) NCs. (I–L) HAADF-STEM images of $NaGdF_4$:Nd/$NaYF_4$ (I), $NaGdF_4$:Nd/$NaYF_4$/$NaGdF_4$:Nd,Yb,Er (J) and $NaGdF_4$:Nd/$NaYF_4$/$NaGdF_4$:Nd,Yb,Er/$NaYF_4$ (K, L) NCs.

sandwich structure (bright-dark-bright-dark) can be observed from the contrast, combined with the statistical line profile analysis of image gray level (yellow line), we can confirm that the C/S1/S2/S3 NCs have been obtained as designed.

In order to achieve the 800-nm excited dual-model DC and UC luminescence, we first demonstrate the important role of Nd^{3+} in the Nd^{3+}, Yb^{3+}, Er^{3+} tri-doped $NaGdF_4$ NCs for UC emission. Since Yb^{3+} ions have no intrinsic absorbency around 800 nm, $NaGdF_4$:Yb,Er NCs were employed as the reference samples in the measurement. Significantly, we found that 0.5% Nd^{3+} doped NCs ($NaGdF_4$:20Yb, 2Er,0.5Nd) was the optimal concentration and showed a nearly 10 fold enhancement on the green UC emission peak of the Er^{3+} as compared with the $NaGdF_4$:20Yb,2Er samples under the 800-nm excitation (Figure 3A). UC emission gradually decreased with the increasing of Nd^{3+} concentration from 0.5% to 2%, indicating that the increased Nd^{3+} doping amount can quench the UC process although the total photon absorbance at 800 nm can be raised. On the other hand, the doping concentration for the DC emission core ($NaGdF_4$:XNd) was also optimized at 5% (Figure S4). Furthermore, suppressing the energy transfer between the DC and UC process is also one of the most important key factors to achieve efficient dual-model luminescence under the same NIR excitation. Almost no DC emission could be observed when 5.5% Nd^{3+}, 20%Yb^{3+}, 2%Er^{3+} was randomly doped in the $NaGdF_4$ matrix (Figure 3B). When the Nd^{3+}, Yb^{3+} and Er^{3+} were doped in two adjacent separate layers ($NaGdF_4$: 5Nd/$NaGdF_4$:20Yb,2Er,0.5Nd), the DC emission intensity was only half compared with the $NaGdF_4$:5Nd/$NaYF_4$/$NaGdF_4$:20Yb,2Er, 0.5Nd NCs involving of the $NaYF_4$ insert layer (Figure 3B). Therefore, we can conclude that inserting of $NaYF_4$ layer is an effective way to switch off the energy transfer between UC and DC processes.

Dual-mode UC and DC luminescence could be obtained by the cooperation of each layer. Upon NIR excitation around 800 nm, C/S1/S2/S3 exhibit characteristic UC and DC emission peaks of Er^{3+} [525 nm ($^2H_{11/2} \rightarrow {}^4I_{15/2}$), 540 nm ($^4S_{3/2} \rightarrow {}^4I_{15/2}$) and 650 nm ($^4F_{9/2} \rightarrow {}^4I_{15/2}$)] and Nd^{3+} [862, 892 nm ($^4F_{3/2} \rightarrow {}^4I_{9/2}$)], respectively (Figure 3C). By comparing the luminescence intensity evolution during our synthesis (Figure 3D), the strongest UC emission was observed in $NaGdF_4$:Nd/$NaYF_4$/$NaGdF_4$:Nd,Yb,Er/$NaYF_4$ C/S1/S2/S3 NCs which is about 20 times stronger than that of NCs without the passivation $NaYF_4$ layer (shell3). In contrast, $NaGdF_4$:Nd/$NaYF_4$ shows the optimal DC emission, which is about 1.2 times stronger than that of C/S1/S2/S3 NCs. This result is reasonable because partial 800-nm light source could be blocked and absorbed by the UC layer before reaching the DC core. It should be noted that $NaGdF_4$:Nd NCs can also exhibit very weak UC emission around 525 and 585 nm under the 800-nm excitation, which can be attributed to the $^2K_{13/2}$, $^4G_{7/2} \rightarrow {}^4I_{9/2}$ and $^4G_{5/2}$,$^2G_{7/2} \rightarrow {}^4I_{9/2}$ transitions of Nd^{3+}. This weak UC emission of Nd^{3+} can be neglected after overcoated with the $NaGdF_4$:Nd,Yb,Er/$NaYF_4$ UC layers. Furthermore, the UC emission intensity excited under exited 800 nm is still weaker than that exited under 980 nm (Figure S9A), which means that there is still large promotion space to develop the high efficiency 800 nm excited UC nanomaterials through delicate design and optimization for the core/shell nanostructure.

Discussion

In order to verify the feasibility for *in-vitro* and *in-vivo* bioimaging, the $NaGdF_4$:Nd/$NaYF_4$/$NaGdF_4$:Nd,Yb,Er/$NaYF_4$ C/S1/S2/S3 NCs were then transferred from the organic phase to the aqueous phase by modifying of the amphiphile phospholipids reported by Lu et al[37]. It was found that the green NIR-to-Visible UC luminescence was still visible to the naked eyes after the phase transfer (Figure 4A). By comparison, the phase transfer has less effect on the NIR-to-NIR DC luminescence (less than 25%) (Figure 4A). To determine whether the obtained NCs can be used for cellular imaging by using 800-nm excited green UC emission, we have performed *in-vitro* cellular bioimaging using human lymphocytes cells (suspension cell). After incubation with 0.2 mg/mL $NaGdF_4$:Nd/$NaYF_4$/$NaGdF_4$:Nd,Yb, Er/$NaYF_4$ C/S1/S2/S3 NCs in phosphate-buffered saline (pH 7.4) for 3 h at 37°C, the unbound nanocrystals were washed away, and

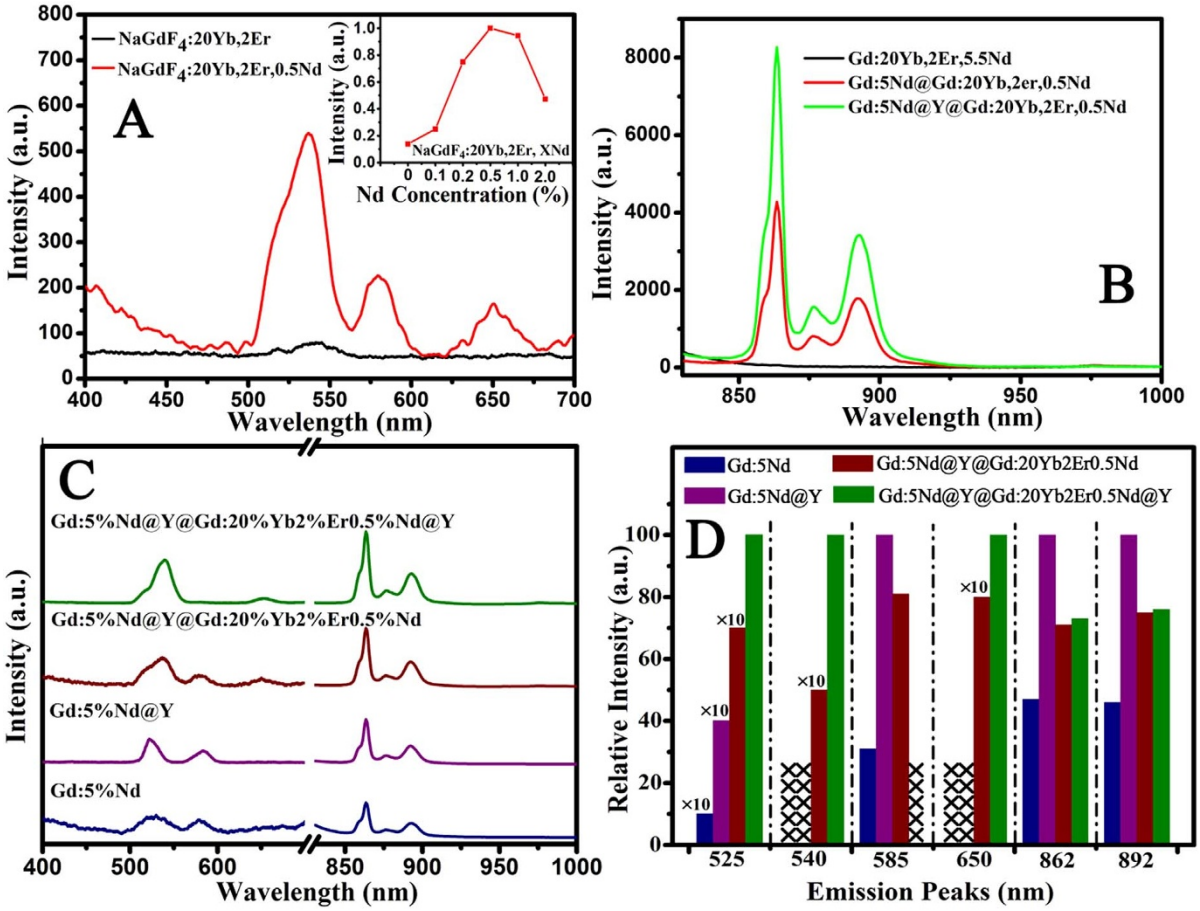

Figure 3 | (A) UC emission spectra of the $NaGdF_4$:20Yb,2Er and $NaGdF_4$:0.5Nd,20Yb,2Er under 800-nm excitation. The inset shows the UC emission intensity of the $NaGdF_4$:Nd,Yb,Er NCs as a function of different Nd^{3+} ion doping concentrations under 800-nm excitation. (B) DC emission spectra of $NaGdF_4$:Nd,Yb,Er, $NaGdF_4$:Nd/$NaGdF_4$:Nd,Yb,Er, and $NaGdF_4$:Nd/$NaYF_4$/$NaGdF_4$:Nd,Yb,Er NCs under 800-nm excitation. (C), (D) UC and DC emission spectra of $NaGdF_4$:Nd core, $NaGdF_4$:Nd/$NaYF_4$, $NaGdF_4$:Nd/$NaYF_4$/$NaGdF_4$:Nd,Yb,Er, $NaGdF_4$:Nd/$NaYF_4$/$NaGdF_4$:Nd,Yb,Er/$NaYF_4$ NCs and corresponding comparison of the relative emission intensity at different emission positions.

the living cells were imaged using 800-nm excitation. Cellular uptake of the NCs can be clearly observed from the merged bright-field and UC signal of cells (Figure 4B–D). Local spectral analysis of the overall cell stained by the NCs confirms that the origin of the cellular luminescence signal is from our NCs (Figure 4E).

The heat effect and penetration depth of UC and DC dual-model nanoprobe under 800-nm excitation, which are two of the most important factors for bioapplications, were also systematic investigated compared with the traditional 980-nm excitation source. It can be seen that the heat effect of 800-nm light is obviously lower than that of 980-nm at the same power density (Figure 5A). When the power density was set at 6 W/cm^2, the temperature in the irradiated area was increased to nearly 60°C in 2 minutes. However, in the case of the 800-nm laser excitation, this value was as low as 49.8°C after the same time duration of irradiation. Furthermore, the degree of burns caused by 980-nm laser is obviously more serious than that of 800-nm at the same power density, serious blistered was observed resulting from the heat effect of 980-nm excitation (Figure S7). The penetration depth of 800 and 980-nm excitations were also studied by checking the power decay of excitation with different tissue depth. It can be seen that the decay rate of 800-nm light is also slower than that of 980-nm (Figure 5B). The half decay of the power of 980-nm is only about 3 mm when the initial power is set at 1.7 W, which is much lower than that of the 800-nm (~5.5 mm). To sum up, we can confirm that the 800-nm excitation source is more suitable for the *in-vivo* applications. As a proof-of-concept experiment, we imbedded the modified $NaGdF_4$:Nd/$NaYF_4$/$NaGdF_4$:Nd,Yb,Er/$NaYF_4$ C/S1/S2/S3 NCs into pork muscle tissue at varied depths (0–15 mm) to investigate the bioimaging feasibility by a modified *in-vivo* imaging system. Duo to the deep tissue penetration of NIR light, the effective depth penetration for the NIR (808 nm)-to-NIR (860–895 nm) DC emission of $NaGdF_4$:Nd/$NaYF_4$/$NaGdF_4$:Nd,Yb,Er/$NaYF_4$ C/S1/S2/S3 NCs was systematic compared with traditional NIR (980 nm)-to-NIR (808 nm) UC $NaGdF_4$:Yb,Tm/$NaYF_4$ (Figure S9B, the efficiency is about 0.4 ± 0.15%). As shown in Figure 5C, the NCs can be detected even at a depth of 15 mm under an excitation power density of approximately 1 W/cm^2. Under identical experimental settings, however, when traditional NIR (980 nm)-to-NIR (808 nm) UC $NaGdF_4$:Yb,Tm/$NaYF_4$ was used as a biomarker agent, the signals are much weaker than that of the C/S1/S2/S3 NCs at the same tissue depth, especially at the deep muscle tissue (>10 mm). To demonstrate the capability of the NIR (800 nm)-to-NIR (860–895 nm) DC for *in-vivo* imaging, 0.2 ml of 5 mg/mL water soluble NCs was imbued to stomach of nude mouse by using gastric syringe. A clear high-contrast luminescence image was observed, almost no auto-fluorescence was observed elsewhere (Figure 5D). It is worthy to note that the DC signal from C/S1/S2/S3 NCs can still be detected even from the back side of the mouse (Figure 5D), suggesting that the 800-nm excited low heat-effect UC and DC dual-mode nanoprobe not only can be used for the NIR (800 nm)-to-Visible (540 nm) *in-vitro* bioimaging but also show great penetration capability in the "NIR biological window".

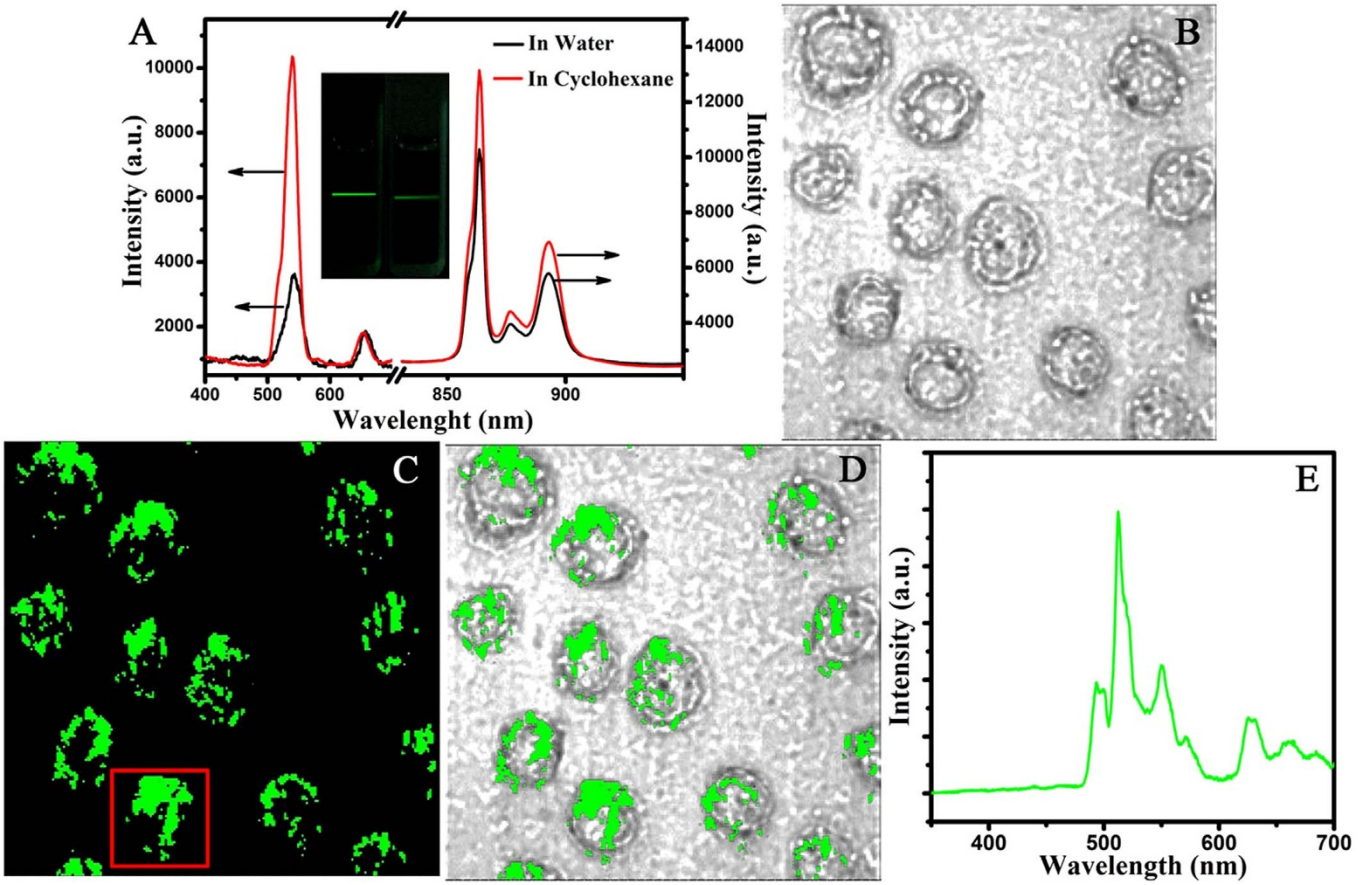

Figure 4 | (A) Calibrated UC and DC emissions and photographs of $NaGdF_4$:Nd/$NaYF_4$/$NaGdF_4$:Nd,Yb,Er/$NaYF_4$ dispersed in hexane (red) and water (black) under 800-nm excitation. High contrast *in-vitro* bioimaging results under 800-nm excitation: (B) bright-field image of human lymphocytes cells labelled with the $NaGdF_4$:Nd/$NaYF_4$/$NaGdF_4$:Nd,Yb,Er/$NaYF_4$ NCs; (C) Corresponding NIR-to-Visible UC imaging result. (D) Merged bright-field and UC imaging result. (E) Local spectral analysis of a single cell (marked with red square in C) labelled with the NCs. The celluar images and spectrum were collected under excitation with 808 nm CW laser and the focused power was about 500 mW.

In conclusion, $NaGdF_4$:Nd/$NaYF_4$/$NaGdF_4$:Nd,Yb,Er/$NaYF_4$ C/S1/S2/S3 NCs were well designed and synthesized, each of the parts assume respective role and work together to achieve dual-mode UC and DC luminescence upon the low heat effect 800-nm excitation. Nd^{3+}, Yb^{3+}, Er^{3+} tri-doped $NaGdF_4$:Nd,Yb,Er UC layer [NIR (800 nm)-to-Visible (540 nm)] with a constitutional efficient 800-nm excitable property were achieved for the *in-vitro* bioimaging with a low auto-fluorescence and photo-damage effects. Moreover, typical NIR (800 nm)-to-NIR (860–895 nm) DC luminescence of Nd^{3+} has also been realized with this designed nanostructure. Due to the low heat effect, high penetration depth of the excitation and the high efficiency of the DC luminescence, the *in-vivo* high contrast DC imaging of a whole body nude mouse was achieved. We believe that such dual-mode luminescence NCs can open the door to engineering the excitation and emission wavelengths of NCs and provide a new tool for a wide variety of applications in the fields of bioanalysis and biomedical.

Methods

Materials. Gadolinium (III) chloride anhydrous ($GdCl_3$, 99.99%), yttrium (III) chloride anhydrous (YCl_3, 99.9%), ytterbium (III) chloride anhydrous ($YbCl_3$, 99.9%), erbium (III) chloride anhydrous ($ErCl_3$, 99.9%), thulium (III) chloride anhydrous ($TmCl_3$, 99.9%), sodium trifluoroacetate (Na-TFA, 98%), 1-octadecene (ODE, 90%), oleic acid (OA, 90%), were purchased from Sigma-Aldrich. Sodium hydroxide (NaOH, 96%), ammonium fluoride (NH_4F, 96%) was obtained from Beijing Chemical Reagents Co. Ltd. 1,2-distearoyl-sn-glycero-3-phosphoethanolamine-N-[carboxy(polyethyleneglycol)-2000] (DSPE-PEG-COOH) was purchased from Avanti Polar Lipids. All chemicals were used as received without any further purification.

Preparation of shell precursors. *Y-OA (0.10 M) host precursor.* a mixture of YCl_3 (2.50 mmol), OA (10.0 mL), and ODE (15.0 mL) was loaded in a reaction container and heated at 140°C under vacuum with magnetic stirring for 30 min to remove residual water and oxygen. Then the colorless Y-OA precursor solution (0.10 M) was obtained.

Gd-OA(0.10 M), Nd-OA (0.10 M), Yb-OA (0.10 M), Er-OA (0.10 M) and Tm-OA (0.10 M) precursor. The synthesis of Gd-OA, Nd-OA, Yb-OA, Er-OA and Tm-OA precursor was carried out all the same as that of Y-OA except 2.50 mmol of $GdCl_3$, 2.50 mmol of $NdCl_3$, 2.50 mmol of $YbCl_3$, 2.50 mmol of $ErCl_3$, 2.50 mmol of $TmCl_3$ were used instead of 2.5 mmol of YCl_3, respectively.

Na-TFA-OA precursor. A mixture of Na-TFA (4.0 mmol) and OA (10 mL) was loaded in a container at room temperature under vacuum with magnetic stirring to remove residual water and oxygen. Then the colorless Na-TFA-OA precursor solution (0.40 M) was obtained.

Synthesis of $NaGdF_4$:Nd DC core NCs. The synthesis of the $NaGdF_4$:5%Nd DC core NCs with a size of ~ 10 nm in this work were similar to previously report by van Veggel et *al*[38]. In a typical procedure, $GdCl_3$ (0.95 mmol), $NdCl_3$ (0.05 mmol), OA (4.0 mL) and ODE (15.0 mL) were mixed together and heated to 140°C under vacuum until a clear solution formed, after that, the solution was cooled to room temperature. A solution of NaOH (2.5 mmol) and NH_4F (4.0 mmol) in methanol (10 mL) was added and the mixture was stirred for a few hours. The reaction mixture was then heated at 70°C to remove the methanol. Afterward, the solution was heated to 290°C and maintained for 100 min under a gentle argon flow. Subsequently, the solution was cool down to room temperature and the NCs precipitated, centrifuged and washed twice with ethanol. The NCs were finally dispersed in 10 mL of cyclohexane for further use.

Synthesis of $NaGdF_4$:Nd/$NaYF_4$ C/S1 NCs by using SLBL method. 3.5 mL of the purified $NaGdF_4$:5%Nd DC core NCs solution (~0.25 mmol) was mixed with 4.0 mL of OA and 6.0 mL of ODE. The flask was pumped down at 70°C for 30 min to remove cyclohexane, any residual air. Subsequently, the system was switched to Ar flow and the reaction mixture was further heated to 280°C at a rate of ~ 20°C/min.

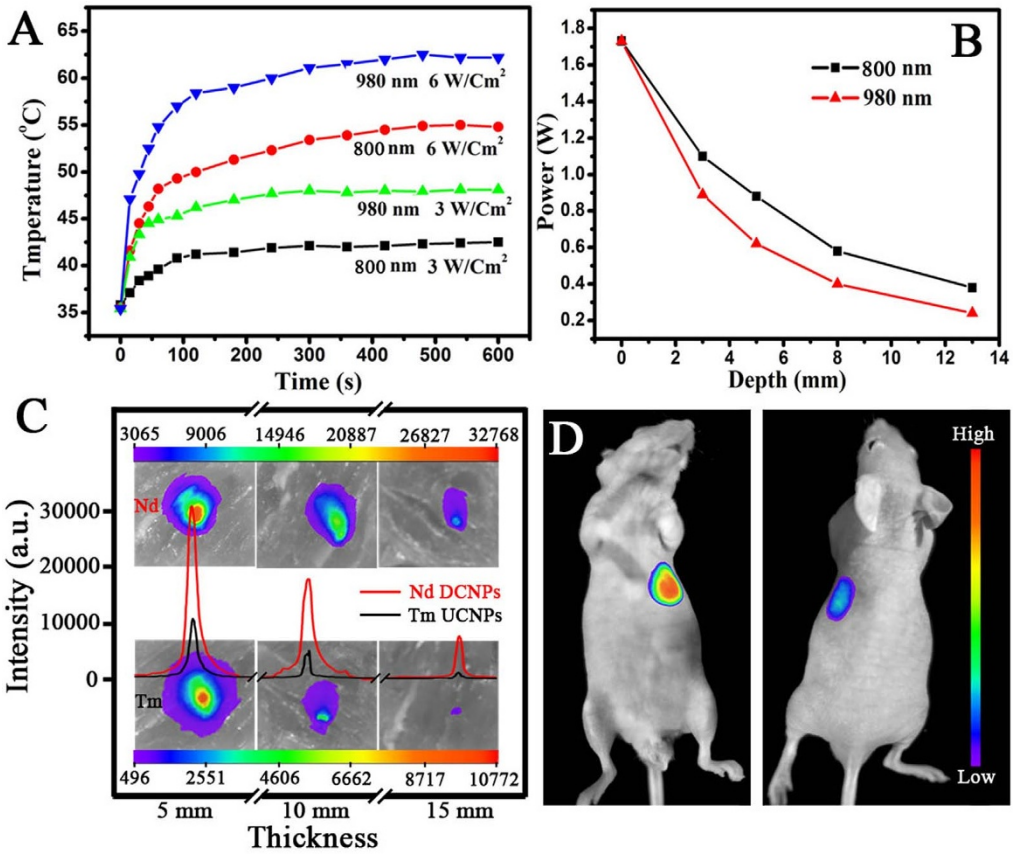

Figure 5 | (A) Time-resolved temperature in the irradiated nude mouse skins during 10 min irradiation of 980- and 800-nm laser as a function of different power density. (B) The decay of excitation power as a function of the penetration depth of tissues. (C) Merged bright-field images with NIR-to-NIR DC emission of $NaGdF_4$:Nd/$NaYF_4$/$NaGdF_4$:Nd,Yb,Er/$NaYF_4$ NCs under 800-nm excitation (top row) and UC emission of traditional $NaGdF_4$:Yb,Tm/$NaYF_4$ NCs under 980-nm excitation (bottom row). Intensities of the signals were also summarized in it. All images were acquired under the same instrumental conditions (power density 1 W/cm^2). (D) *In-vivo* imaging of a nude mouse from the chest side (left) and the back side (right) by imbuing the water soluble $NaGdF_4$:Nd/$NaYF_4$/$NaGdF_4$:Nd,Yb,Er/$NaYF_4$ NCs to stomach.

Then six pairs of Y-OA (0.10 M, 1.0 mL) and Na-TFA-OA (0.40 M, 0.5 mL) host shell precursors were alternately introduced by dropwise addition at 280°C and the time interval between each injection was 15 min. Finally, the obtained $NaGdF_4$:Nd/$NaYF_4$ C/S1 NCs were precipitated and washed as above for core NCs and dispersed in cyclohexane.

Synthesis of $NaGdF_4$:Nd/$NaYF_4$/$NaGdF_4$:Nd,Yb,Er C/S1/S2 NCs by using SLBL method. The Gd-Nd-Yb-Er-OA (0.10 M) shell precursor was firstly obtained from a mixture of Gd-OA (0.10 M), Nd-OA (0.10 M), Yb-OA (0.10 M) and Er-OA (0.10 M) in a 79.5 : 0.5 : 20 : 2 ratio. Then, all of the purified $NaGdF_4$:Nd/$NaYF_4$ C/S1 NCs solution was mixed with 4.0 mL of OA and 6.0 mL of ODE. The flask was pumped down at 70°C for 30 min to remove cyclohexane. Subsequently, the system was switched to Ar flow and the reaction mixture was further heated to 280°C at a rate of ~ 20°C/min. Then eight pairs of Gd-Nd-Yb-Er-OA (0.10 M, 1.0 mL) and Na-TFA-OA (0.40 M, 0.5 mL) host shell precursors were alternately introduced by dropwise addition at 280°C and the time interval between each injection was 15 min. The resultant nanoparticles were precipitated by addition of ethanol, collected by centrifugation, washed with ethanol several times, and re-dispersed in cyclohexane.

Synthesis of $NaGdF_4$:Nd/$NaYF_4$/$NaGdF_4$:Nd,Yb,Er/$NaYF_4$ C/S1/S2/S3 NCs by using SLBL method. The process for overcoating of the outmost $NaYF_4$ passivation layer was the same as the synthesis of the $NaGdF_4$:Nd/$NaYF_4$ C/S1 NCs except that ten pairs of Y-OA (0.10 M, 1.0 mL) and Na-TFA-OA (0.40 M, 0.5 mL) host shell precursors were alternately introduced by dropwise addition.

Transferring $NaGdF_4$:Nd/$NaYF_4$/$NaGdF_4$:Nd,Yb,Er/$NaYF_4$ C/S1/S2/S3 NCs from hexane solution to aqueous. The phase transfer method used in this work were similar to previously report by Lu et *al*[37]. Typically, 1 mL of oleic acid capped NCs in chloroform (10 mg/mL) was mixed with a chloroform solution (1 mL) containing 12.5 mg DSPE-PEG-COOH in a screw-neck glass bottle. Leave the glass bottle open in a fume hood for two days at room temperature to evaporate the chloroform slowly. The obtained mixed film was heated at 75°C for 5 min to completely remove chloroform. Then the film was hydrated with MilliQ water (5 mL), and the NCs became soluble after vigorously sonication, which can be further stirred vigorously at 75°C for 10 min. The solution was transferred to a microtube and centrifuged, the sediment was discarded to remove possible large aggregates. Excess lipids were purified by ultracentrifugation (15000 rpm, 10 min) and washing.

In-vitro and in-Vivo imaging using the obtained NCs. In-vitro cellular imaging was done using Olympus IX71 microscope equipped with the SP 2360 spectrometers and Pro EM CCD camera (Princeton Instruments Inc.). 800-nm CW laser was used as the excitation source, in combination with a short pass optical filter (750 SP from Chroma Corp). *In-vivo* imaging was performed with a modified LB983 NightOWL II (Berthold Technologies GmbH & Co.KG, Germany) using an external 0 ~ 2 W adjustable 800-nm CW laser as the excitation source. 0.2 ml of 5 mg/mL water soluble NCs was imbued to stomach of nude mouse by using gastric syringe. Then the optical whole body images of mice were recorded on the modified LB983 NightOWL II instrument. The animal experimental procedures were approved by Animal Use and Care Administrative Advisory Committees of Laboratory of Advanced Materials, Fudan University. The nude mice were purchased from Shanghai SLAC Laboratory Animal Co., Ltd. (Shanghai, China). All animal experimental procedures were in agreement with institutional animal use and care regulations. Imaging of pork muscle tissue: water-soluble $NaGdF_4$:Nd/$NaYF_4$/$NaGdF_4$:Nd,Yb,Er/$NaYF_4$ C/S1/S2/S3 and $NaGdF_4$:Yb,Tm/$NaYF_4$ were dissolved in warm 1% agarose solution (5 mg/mL). After cooling to the room temperature, the solidified agarose gel containing the NCs were taken and placed into pork muscle tissues at different depths. All animal experimental procedures were in agreement with institutional animal use and care regulations.

Characterization. Transmission electron microscopy (TEM), high-resolution transmission electron microscopy (HRTEM), high-angle annular dark field imaging in the scanning TEM (HAADF-STEM) and electron energy loss spectroscopy (EELS) observations were performed on JEM-2100F transmission electron microscope with an accelerating voltage of 200 kV equipped with a post-column Gatan imaging filter (GIF-Tri-dium). X-ray diffraction (XRD) measurements were carried out at room temperature with a Bruker D8 diffractometer using Cu Kα radiation (wavelength = 1.5406 Å). We characterized the upconversion and downconversion spectra on a Hitachi Fluorescence Spectrometer F4500 instrument and Ocean Optics UV-VIS-NIR CCD (QE65000) equipped with a 800-nm CW laser (20 W/cm^2), respectively. The QYs were test according to our previous report[36]. The heat effect of the laser

sources were recorded on a professional infrared thermal imaging camera (FLIR ThermaCAM A300). All of the as-synthesized NCs were dispersed in hexane to form transparent colloidal solutions with the same particle concentrations (10 mg/mL).

1. Michalet, X. *et al.* Quantum dots for live cells, in vivo imaging, and diagnostics. *Science*, **307**, 538–544 (2005).
2. Resch-Genger, U., Grabolle, M., Cavaliere-Jaricot, S., Nitschke, R. & Nann, T. Quantum dots versus organic dyes as fluorescent labels. *Nat. Methods* **5**, 763–775 (2008).
3. Becker, A. *et al.* Receptor-targeted optical imaging of tumors with near-infrared fluorescent ligands. *Nat. Biotechnol.* **19**, 327–331 (2001).
4. Weissleder, R. A clearer vision for in vivo imaging. *Nat. Biotechnol.* **19**, 316–317 (2001).
5. Smith, A. M., Mancini, M. C. & Nie, S. Bioimaging: second window for in vivo imaging. *Nat. Nanotechnol.* **4**, 710–711 (2009).
6. Li, Z., Zhang, Y. & Jiang, S. Multicolor core/shell-structured upconversion fluorescent nanoparticles. *Adv. Mater.* **20**, 4765–4769 (2008).
7. Cheng, L. *et al.* Facile Preparation of Multifunctional Upconversion Nanoprobes for Multimodal Imaging and Dual-Targeted Photothermal Therapy. *Angew. Chem. Int. Ed.* **50**, 7385–7528 (2011).
8. Liu, Q. *et al.* Sub-10 nm Hexagonal Lanthanide-Doped $NaLuF_4$ Upconversion Nanocrystals for Sensitive Bioimaging in Vivo. *J. Am. Chem. Soc.* **133**, 17122–17125 (2011).
9. Hong, G. *et al.* In Vivo Fluorescence Imaging with Ag_2S Quantum Dots in the Second Near-Infrared Region. *Angew. Chem. Int. Ed.* **51**, 9818–9821 (2012).
10. Gu, Y.-P., Cui, R., Zhang, Z.-L., Xie, Z.-X. & Pang, D.-W. Ultrasmall Near-Infrared Ag2Se Quantum Dots with Tunable Fluorescence for in Vivo Imaging. *J. Am. Chem. Soc.* **134**, 79–82 (2012).
11. Welsher, K. *et al.* A route to brightly fluorescent carbon nanotubes for near-infrared imaging in mice. *Nat. Nanotechnol.* **4**, 773–780 (2009).
12. Tian, G. *et al.* Mn^{2+} Dopant-Controlled Synthesis of $NaYF_4$:Yb/Er Upconversion Nanoparticles for in vivo Imaging and Drug Delivery. *Adv. Mater.* **24**, 1226–1231 (2012).
13. Wang, Y.-F. *et al.* Rare-Earth Nanoparticles with Enhanced Upconversion Emission and Suppressed Rare-Earth-Ion Leakage. *Chem. Eur. J.* **18**, 5558–5564 (2012).
14. Johnson, N. J. J., Korinek, A., Dong, C. & van Veggel, F. C. J. M. Self-Focusing by Ostwald Ripening: A Strategy for Layer-by-Layer Epitaxial Growth on Upconverting Nanocrystals. *J. Am. Chem. Soc.* **134**, 11068–11071 (2012).
15. Ju, Q. *et al.* Amine-Functionalized Lanthanide-Doped $KGdF_4$ Nanocrystals as Potential Optical/Magnetic Multimodal BioProbes. *J. Am. Chem. Soc.* **134**, 1323–1330 (2012).
16. Su, Q. *et al.* The Effect of Surface Coating on Energy Migration-Mediated Upconversion. *J. Am. Chem. Soc.* **134**, 20849–20857 (2012).
17. Zhang, F. *et al.* Direct Imaging the Upconversion Nanocrystal Core/Shell Structure at the Subnanometer Level: Shell Thickness Dependence in Upconverting Optical Properties. *Nano Lett.* **12**, 2852–2858 (2012).
18. Jayakumar, M. K. G., Idris, N. M. & Zhang, Y. Remote activation of biomolecules in deep tissues using near-infrared-to-UV upconversion nanotransducers. *Proc. Natl. Acad. Sci.* **109**, 8483–8488 (2012).
19. Vetrone, F., Naccache, R., Mahalingam, V., Morgan, C. G. & Capobianco, J. A. The Active-Core/Active-Shell Approach: A Strategy to Enhance the Upconversion Luminescence in Lanthanide-Doped Nanoparticles. *Adv. Funct. Mater.* **19**, 2924–2929 (2009).
20. Chen, G. *et al.* (alpha-$NaYbF4:Tm^{3+}$)/CaF_2 Core/Shell Nanoparticles with Efficient Near-Infrared to Near-Infrared Upconversion for High-Contrast Deep Tissue Bioimaging. *ACS Nano* **6**, 8280–8287 (2012).
21. Liu, J., Bu, W., Pan, L. & Shi, J. NIR-Triggered Anticancer Drug Delivery by Upconverting Nanoparticles with Integrated Azobenzene-Modified Mesoporous Silica. *Angew. Chem. Int. Ed.* **52**, 4375–4379 (2013).
22. Liu, X. *et al.* Breakthrough in concentration quenching threshold of upconversion luminescence via spatial separation of the emitter doping area for bio-applications. *Chem. Commun.* **47**, 11957–11959 (2011).
23. Kumar, R., Nyk, M., Ohulchanskyy, T. Y., Flask, C. A. & Prasad, P. N. Combined Optical and MR Bioimaging Using Rare Earth Ion Doped $NaYF_4$ Nanocrystals. *Adv. Funct. Mater.* **19**, 853–859 (2009).
24. Hou, Z. *et al.* Preparation and Luminescence Properties of YVO_4:Ln and Y(V, P)O_4:Ln (Ln = Eu^{3+}, Sm^{3+}, Dy^{3+}) Nanofibers and Microbelts by Sol-Gel/Electrospinning Process. *Chem. Mater.* **20**, 6686–6696 (2008).
25. Huo, Z., Chen, C., Chu, D., Li, H. & Li, Y. Systematic synthesis of lanthanide phosphate nanocrystals. *Chem. Eur. J.* **13**, 7708–7714 (2007).
26. Lee, H. J., Park, J.-U., Choi, S., Son, J. & Oh, M. Synthesis and Photoluminescence Properties of Eu^{3+}-Doped Silica@Coordination Polymer CoreShell Structures and Their Calcinated Silica@Gd_2O_3:Eu and Hollow Gd_2O_3:Eu Microsphere Products. *Small* **9**, 561–569 (2013).
27. Zhan, Q. *et al.* Andersson-Engels, S. Using 915 nm Laser Excited Tm^{3+}/Er^{3+}/Ho^{3+}-Doped $NaYbF_4$ Upconversion Nanoparticles for in Vitro and Deeper in Vivo Bioimaging without Overheating Irradiation. *ACS Nano* **5**, 3744–3757 (2011).
28. Li, M. *et al.* Controllable energy transfer in fluorescence upconversion of NdF_3 and $NaNdF_4$ nanocrystals. *Opt. Express* **18**, 3364–3369 (2010).
29. Singh, S., Smith, R. G. & Van Uiter, L. G. Stimulated-Emission Cross-Section and Fluorescent Quantum Efficiency of Nd^{3+} in Yttrium Aluminum Garent at Room-Temperature. *Phys. Rev. B* **10**, 2566–2572 (1974).
30. Wang, X. F. *et al.* Enhancement of blue emission in beta-$NaYbF_4$:Tm^{3+}/Nd^{3+} nanophosphors synthesized by nonclosed hydrothermal synthesis method. *Appl. Phys. B-lasers. O* **101**, 623–629 (2010).
31. Wang, X., Xiao, S., Bu, Y. & Ding, J. W. Upconversion properties of Nd^{3+}-Yb^{3+}-Ho^{3+}-doped beta-$Na(Y_{1.5}Na_{0.5})F_6$ powders. *J. Alloy. Compd.* **477**, 941–945 (2009).
32. Li, A.-H. *et al.* Visible and ultraviolet upconversion emission in $LiNbO_3$ triply doped with Tm^{3+}, Yb^{3+}, and Nd^{3+}. *J. Appl. Phys.* **105**, 013536 (2009).
33. Wetter, N. U. & Deana, A. M. Diode-side-pumped Nd:$YLiF_4$ laser emitting at 1053 nm with 53.6% optical efficiency and diffraction-limited beam quality. *Laser Physics Letters* **10**, 035807 (2013).
34. Chen, D., Wang, Y., Yu, Y., Liu, F. & Huang, P. Sensitized thulium ultraviolet upconversion luminescence in Tm^{3+}/Yb^{3+}/Nd^{3+} triply doped nanoglass ceramics. *Opt. Lett.* **32**, 3068–3070 (2007).
35. Chen, G. *et al.* Core/Shell $NaGdF_4$:Nd^{3+}/$NaGdF_4$ Nanocrystals with Efficient Near-Infrared to Near-Infrared Downconversion Photoluminescence for Bioimaging Applications. *ACS Nano* **6**, 2969–2977 (2012).
36. Li, X. *et al.* Successive Layer-by-Layer Strategy for Multi-Shell Epitaxial Growth: Shell Thickness and Doping Position Dependence in Upconverting Optical Properties. *Chem. Mater.* **25**, 106–112 (2013).
37. Li, L.-L. *et al.* Biomimetic Surface Engineering of Lanthanide-Doped Upconversion Nanoparticles as Versatile Bioprobes. *Angew. Chem. Int. Ed.* **51**, 6121–6125 (2012).
38. Johnson, N. J. J., Oakden, W., Stanisz, G. J., Scott Prosser, R. & van Veggel, F. C. J. M. Size-Tunable, Ultrasmall $NaGdF_4$Nanoparticles: Insights into Their T1 MRI Contrast Enhancement. *Chem. Mater.* **23**, 3714–3722 (2011).
39. Xie, X. *et al.* Mechanistic Investigation of Photon Upconversion in Nd^{3+}-Sensitized Core−Shell Nanoparticles. *J. Am. Chem. Soc.* **135**, 12608–12611 (2013).
40. Shen, J. *et al.* Engineering the Upconversion Nanoparticle Excitation Wavelength: Cascade Sensitization of Tri-doped Upconversion Colloidal Nanoparticles at 800 nm. *Adv. Opt. Mater.* **1**, 644–650 (2013).
41. Wang, Y. F. *et al.* Nd^{3+}-Sensitized Upconversion Nanophosphors: Efficient In Vivo Bioimaging Probes with Minimized Heating Effect. *ACS Nano* **7**, 7200–7206 (2013).

Acknowledgments

The work was supported by China National Key Basic Research Program (973 Project) (No. 2013CB934100, 2012CB224805, 2010CB933901), the NSFC (grant no. 21322508,21101029, 21273041, 21210004), Shanghai Rising-Star Program (12QA1400400), the State Key Laboratory of Pollution Control and Resource Reuse Foundation (no. PCRRF12001), and the Fudan Startup Foundation for Advanced Talents.

Author contributions

X.L., F.Z. and D.Z. contributed to the conception and design of the experiment, analysis of the data and writing the manuscript. R.W. assisted X.L. by carrying out synthesis of materials, optical and structural characterizations of the synthesized products. X.L. and R.W. contributed equally to this work. L.Z., D.S. and C.Y. assisted X.L. by performing the experiments of *in-vitro* and *in-vivo* bio-imaging. All authors reviewed the manuscript.

Additional information

Supplementary information accompanies this paper at http://www.nature.com/scientificreports

Competing financial interests: The authors declare no competing financial interests.

How to cite this article: Li, X.M. *et al.* Nd^{3+} Sensitized Up/Down Converting Dual-Mode Nanomaterials for Efficient *In-vitro* and *In-vivo* Bioimaging Excited at 800 nm. *Sci. Rep.* **3**, 3536; DOI:10.1038/srep03536 (2013).